Supplementary Information (SI) for Environmental Science: Nano.

Ce/W-MIL-88B(Fe) Photo-Fenton Material Achieving Synchronous Arsenate Uptake and Nitrite Resourcing: Unexpected Role of Arsenate in Boosting Photo-Fenton Activity

Xi Chen[a,c], Jiabin Gao[a], Wei He[a], Hanxiao Liu[d,e], Mengyuan Wu[a], Meng Qi[a], Lijuan Yang[a], Feng Liu[a], Runlong Hao*[,a,b]

[a] *Hebei Key Lab of Power Plant Flue Gas Multi-Pollutants Control, Department of Environmental Science and Engineering, North China Electric Power University, Baoding, 071003, PR China.*

[b] *MOE Key Laboratory of Resources and Environmental Systems Optimization, College of Environmental Science and Engineering, North China Electric Power University, Beijing, 102206, PR China.*

[c] *State Key Laboratory of Urban Water Resource and Environment (SKLUWRE), School of Environment, Harbin Institute of Technology, Harbin150090, P. R. China*

[d] *Zhejiang Feida Environmental Science & Technology Co., Ltd., Zhuji 311800, China*

[e] *Huazhong University of Science and Technology, Wuhan 430074, China*

[*] *Corresponding authors E-mail: hrl_ncepu@hotmail.com.*

Text S1. Chemicals and regents

All chemicals and reagents were purchased directly without further purification. All solutions were prepared by using deionized (DI) water obtained from Milli-Q ultrapure water purification system (Millipore, Billerica, MA). Iron chloride hexahydrate ($FeCl_3 \cdot 6H_2O$, 99%, Macklin Co., China.), cerium nitrate ($Ce(NO_3)_2 \cdot 6H_2O$, 99%, Macklin Co., China.), terephthalic acid (H_2BDC, $C_8H_6O_4$, 99%, Macklin Co., China.), and N, N-dimethylformamide (C_3H_7NO, 99%, Aladdin Co., China.) were used to synthesize Ce/W-MIL-88B(Fe) via hydrothermal method. Ethanol (C_2H_5OH, 99.7%, Damao Technology Co., China) and DI water were used as washing solutions. Sodium nitrite ($NaNO_2$, 99%, Aladdin Co., China.) and arsenate (As(V), 1000 ug/mL in water, Aladdin Co., China.) were used as the target pollutants. Potassium peroxymonosulfate (PMS, $2KHSO_5 \cdot KHSO_4 \cdot K_2SO_4$, 42%-46% $KHSO_5$ basis, Aladdin Co., China.) was used as the oxidant. Sodium hydroxide (NaOH, 99%, Damao Co. Technology Co., China.) and HCl (36-38%wt, Damao Co. Technology Co., China.) were used to adjust the pH of mixture solution. HCl, thiourea (CH_4N_2S, 99%, Kermel Co., China.) and L-ascorbic acid ($C_6H_8O_6$, 99.7%, Kermel Co., China.) were used as the reducing solutions to test As(V) concentration. Tert-butyl alcohol ($C_4H_{10}O$, 99%, Aladdin Co., China.), methanol (MeOH, CH_4O, 99.5%, Aladdin Co., China.), L-ascorbic acid and furfuryl alcohol ($C_5H_6O_2$, 98%, Aladdin Co., China.) were used as the free radical quenchers to determine their contributions to NO_2^- conversion. A commercial polytetrafluoroethylene (PTFE) microfiltration membrane (Φ=50 mm, pore diameter=0.45 μm) was used to collect products by filtration.

Text S2. Photocatalysis and adsorption experiments

The photocatalytic performance of Ce/W-MIL-88B(Fe) on NO_2^- oxidation was tested under simulated sunlight irradiation with using a 300 W xenon lamp (CEL-PE300L-3A, Education Au-Light Technology Co., China) at 25 ^oC. 0.25 $g \cdot L^{-1}$ photocatalysts were added into a 100 mL solution containing 15 mM $NaNO_2$. The pH of the solution was adjusted by using 1 mM HCl or 1 mM NaOH. Then, the suspension was stirred in darkness for 30 min before visible light irradiation; thereafter, 5 mM PMS was added into the solution. The mixed solution was magnetically stirred for 1 h at 300 rpm. The concentration of NO_2^- was continuously measured by an ultraviolet spectrophotometer (GB/T 5750.5-2006), for each test 0.02 mL solution was taken to be tested. Sulfanilic acid solution (2 mL, 4 $g \cdot L^{-1}$) and naphthalene hydrochloride ethylenediamine solution (1 mL, 2 $g \cdot L^{-1}$) were added into the sample solutions, and then diluted the solution to 50 mL and mixed well. After standing for 15 min, the NO_2^- concentration in the solution was determined based on its absorbance at 538 nm.

The form of As(V) in aqueous is always AsO_4^{3-}, thus we used the standard As solution as the stock solution to prepare the experimental As(V) solution in the concentration range of 10-110 $mg \cdot L^{-1}$. The pH of the As(V) solution was adjusted by using 1 mM HCl or 1 mM NaOH. The As(V) adsorption batch test was carried out in a 100 mL solution by adding 0.025 g Ce/W-MIL-88B(Fe). Then, the mixed solution was stirred at 300 rpm for 12 h to achieve adsorption equilibrium. Finally, we used a 0.45 μm syringe filter (polyethersulfone ultrafiltration membrane, Jin Teng, China) to filter the solution, and determined the As(V) concentration by using an atomic fluorescence spectrometry (AFS-9230, Jitian Co., China) with a carrier solution of 5% HCl and a reducing solution of 5% thiourea and 5% ascorbic acid. As(V) adsorption kinetics were calculated according to the pseudo-first-order, pseudo-second-order and intra-particle diffusion models to reveal the adsorption behavior and mechanism of As(V) adsorption. In addition, the adsorption isotherms based on the Langmuir and Freundlich isotherm models were established to determine the As(V) adsorption capacity. All experiments were repeated at least for three times, and the average values were used to calculate the NO_2^- oxidation efficiency or the As(V)

adsorption efficiency via eq. S1:

$$\eta = 1 - \left(\frac{C_{in}}{C_{out}}\right) \times 100\% \quad \text{(S1)}$$

where η is the NO_2^- oxidation efficiency or the As(V) adsorption efficiency; C_{in} and C_{out} are the initial and final concentrations of NO_2^- or As(V), $mg \cdot L^{-1}$.

Text S3. Characterization

The surface morphologies and microstructures of the composite materials were imaged with scanning electron microscopy (SEM; Zeiss Ultra 60, Carl Zeiss, Germany), transmission electron microscopy (TEM; JEM-2100, JEOL, Japan), and energy-dispersive X-ray spectroscopy (EDS; XFlash 5060FQ, Bruker, Germany). The X-ray diffraction (XRD; D8 ADVANCE, Bruker) patterns were performed using an X-ray spectrometer with a Cu Kα radiation at a scan rate of 10° min^{-1} from 20 to 90°. The surface chemical composition analysis of the composite materials was recorded by X-ray photoelectron spectroscopy (XPS; ESCALAB 250, Thermo Fisher Scientific, USA) and valence band XPS (VB-XPS; ESCALAB 250, Thermo Fisher Scientific, USA) with an Al Kα source (1486.6 eV). Low-temperature electron spin resonance (ESR; EMXPLUS, Bruker) was used to detect the radicals. The surface charge of the composite materials was tested by a Zeta potentiometer (Zetasizer Nano ZS90, Malvern Panalytical, UK). Photoluminescence spectra were performed on a fluorescence spectrometer (PL; FLS1000, Edinburgh, UK). UV-Vis diffuse reflection spectroscopy (DRS; UV3600IPLUS, Shimadzu, Japan) analysis was conducted on a UV-Vis spectrophotometer with a wavelength range of 250-800 nm. A surface area and pore size analyzer (SA 3100, Beckman Coulter, USA) was used to measure the porosity of the catalysts. The pore volume and surface area were determined by the Brunauer–Emmett–Teller method (BET; TriStar II 3020, Micromeritics, USA) with nitrogen adsorption-desorption isotherms. Inductively coupled plasma-mass spectrometry (7700, Agilent Technology Co., USA) was used to determine the Fe and Ce contents in the catalysts, as well as the leached Fe and Ce ions in the reacted solution.

Text S4. XRD Patterns Analyses

XRD patterns of different materials are presented in Figure S2. The main diffraction peaks of Ce-BDC are in the range of 10-30°, and was mainly formed by the combination of Ce-Oxo cluster with oxygen atoms from different H_2BDC and six coordinated water molecules[1]. W-MIL-88B(Fe) is presented in hexagonal symmetric structure (space group: P2c), and the diffraction peaks at 9.22°, 10.50°, 16.58° and 18.20° correspond to the facets (002), (101), (103) and (200), respectively.[2] After Ce-doping, the Ce/W-MIL-88B(Fe) appears in a high crystallization form, which has a similar diffraction peak position to that of the W-MIL-88B(Fe), indicating that Ce doping does not change on the crystal phase structure of W-MIL-88B(Fe). However, the diffraction peak intensities between Ce/W-MIL-88B(Fe) and W-MIL-88B(Fe) are different. The intensity of the facet (200) on Ce/W-MIL-88B(Fe) increases visibly, indicating a crystal orientation trend, which implied that the preferential growth of the defective W-MIL-88B(Fe) crystal structure promoted by in situ Ce-doping.

Text S5. Band Gap Calculation

The band gaps of the composite materials were calculated by eq. S2:

$$\alpha(hv)=A\ (hv-Eg)^{1/2} \quad \text{(S2)}$$

where a, v, A, and Eg represents the absorption coefficient, light frequency, a constant, and the band gap energy, respectively.

$$\Phi\ (eV)=hv\ -\ (E_{Fermi}\ -\ E_{cutoff}) \quad \text{(S3)}$$

where *hv* represents the He I energy of 21.2 eV.

$$E_{VB} = \Phi + E_{MVB}-4.5 \quad \text{(S4)}$$

$$E_{CB} = E_{VB}-E_g \quad \text{(S5)}$$

Text S6. Adsorption Kinetics

To reveal the behavior of As(V) adsorption, the adsorption kinetics were studied based on the pseudo-first-order model, pseudo-second-order model and intra-particle diffusion model. The related parameters are summarized in Table S2. The fitting result shown in Figure S5 indicates that the pseudo-first-order model is not fit. By contrast, as shown in Figure S6, the regression coefficients (R^2) of the pseudo-second-order fitting curve for all materials were close to 1, and the $q_{e,cal}$ values were well agreed with the experimental q_e values, suggesting that pseudo-second-order model was competent to describe the adsorption kinetics of As(V).

In addition, the intra-particle diffusion model was also employed to determine the rate-determining step in As(V) adsorption process. As shown in Figure S7, the As(V) adsorption process can be divided into three linearity plots, i.e. external transfer step, intra-particle diffusion step and final equilibrium step; and the plots of q_t against $t^{1/2}$ were straight lines passing through the origin, indicating that the rate-determining step was pore diffusion rather than boundary layer diffusion.

$$\frac{1}{q_t} = \frac{k_1}{q_{e1} t} + \frac{1}{q_{e1}} \tag{S6}$$

$$\frac{t}{q_t} = \frac{1}{(k_2 q_{e2}^2)} + \frac{t}{q_{e2}} \tag{S7}$$

$$q_t = k_{id} t^{1/2} + I \tag{S8}$$

where k_1 and k_2 are the pseudo-first-order constant and pseudo-second-order constant, respectively; R^2 is the linear correlation coefficient; q_e ($mg \cdot g^{-1}$) represents the adsorption capacity of the adsorbent at equilibrium; q_t ($mg \cdot g^{-1}$) is the adsorption capacity of the adsorbent at time t; K_{id} ($mg \cdot g^{-1} \cdot min^{-1/2}$) denotes the intra-particle diffusion rate constant; and I is the intercept of the intra-particle diffusion model.

Text S7. Adsorption Isotherm

To further determine the As(V) adsorption capacity, the adsorption isotherms were established according to the Langmuir and Freundlich isotherm models, with the initial concentration of As(V) ranging from 0 to 110 $mg \cdot L^{-1}$. Table S3 summarizes the parameters of Langmuir and Freundlich isotherms. As shown in Figure 4e, As(V) adsorption capacity increased constantly with the increase in equilibrium concentration (C_e), and reached saturation in the end, with the maximum adsorption capacity of higher than 181 $mg \cdot g^{-1}$. Moreover, the R^2 of Langmuir model was higher than that of Freundlich model, so As(V) adsorption process followed the Langmuir model. Herein, the adsorption process followed the Langmuir model, meaning that As(V) adsorption was monolayer adsorption and had a constant site energy distribution.

$$q_e = \frac{q_{max} K_L C_e}{1 + K_L C_e} \tag{S9}$$

$$q_e = K_F C_e^{1/n} \tag{S10}$$

where C_e ($mg \cdot L^{-1}$) represents the equilibrium concentration of As(V) in solution; q_e ($mg \cdot g^{-1}$) is the amount of adsorbed As(V) per unit mass of Ce/W-MIL-88B(Fe); K_L ($L \cdot mg^{-1}$) denotes Langmuir affinity constant related to the energy of adsorption; q_{max} ($mg \cdot g^{-1}$) is the maximum adsorption capacity; K_F ($mg/g \cdot (L/mg)^{1/n}$) represents the Freundlich constant related to the adsorption affinity; and n is a dimensionless indicator related to the adsorbent surface heterogeneity.

Text S8. The N/As selectivity

The synergistic catalytic/adsorption experiments were performed to investigate the N/As selectivity of Ce/W-MIL-88B(Fe). The N selectivity (S_N) and As(V) selectivity (S_{As}) are calculated as follows:

$$S_N = \frac{O_N}{O_A} \tag{S11}$$

where O_N is the oxidation efficiency of Ce/W-MIL-88B(Fe) for NO_2^-. O_A is the oxidation efficiency of Ce/W-MIL-88B(Fe) for NO_2^- under synergistic NO_2^- catalytic oxidation and As(V) adsorption.

$$S_{As} = \frac{R_{As}}{R_A} \tag{S12}$$

where R_{As} is the removal efficiency of Ce/W-MIL-88B(Fe) for As(V). R_A is the oxidation efficiency of Ce/W-MIL-88B(Fe) for NO_2^- under synergistic NO_2^- catalytic oxidation and As(V) adsorption.

Figure S1. Schematic illustration of the synthesis process of Ce/W-MIL-88B(Fe)

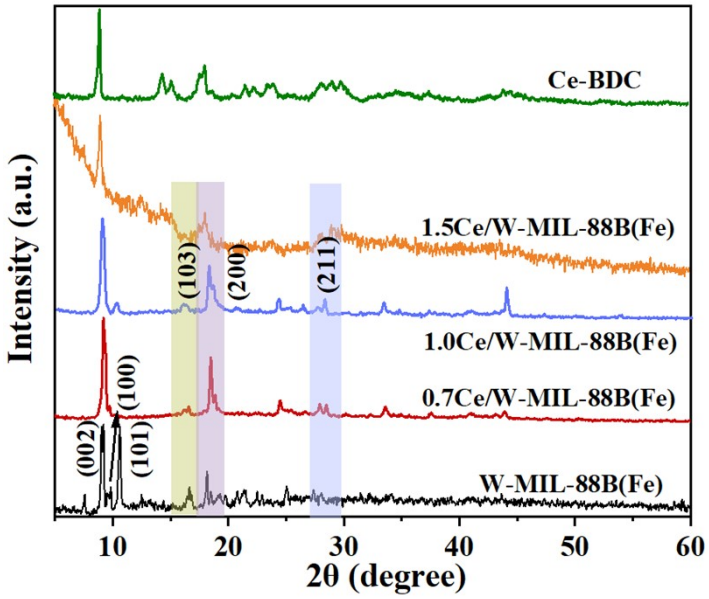

Figure S2. XRD patterns of W-MIL-88B(Fe), Ce-BDC and Ce/W-MIL-88B(Fe).

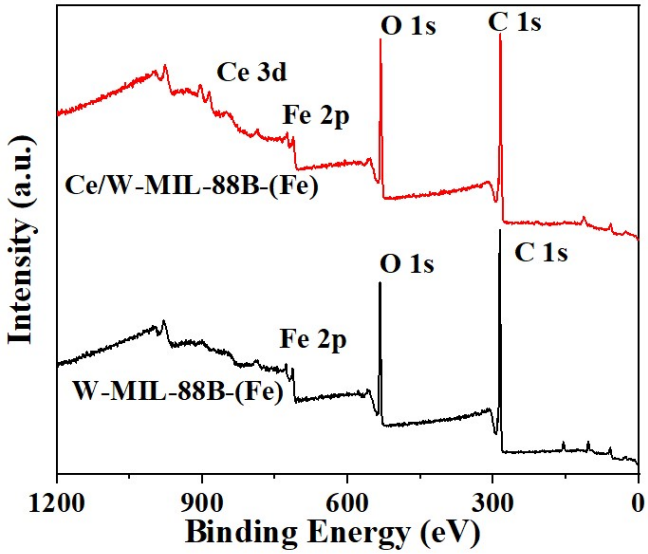

Figure S3. The wide-scan XPS spectra of Ce/W-MIL-88B(Fe) and W-MIL-88B(Fe).

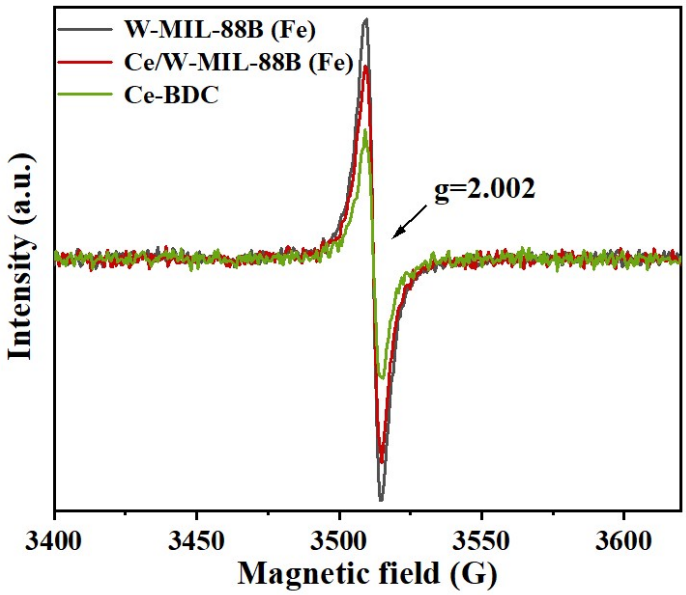

Figure S4. ESR profiles of W-MIL-88B(Fe), Ce-BDC and Ce/W-MIL-88B(Fe).

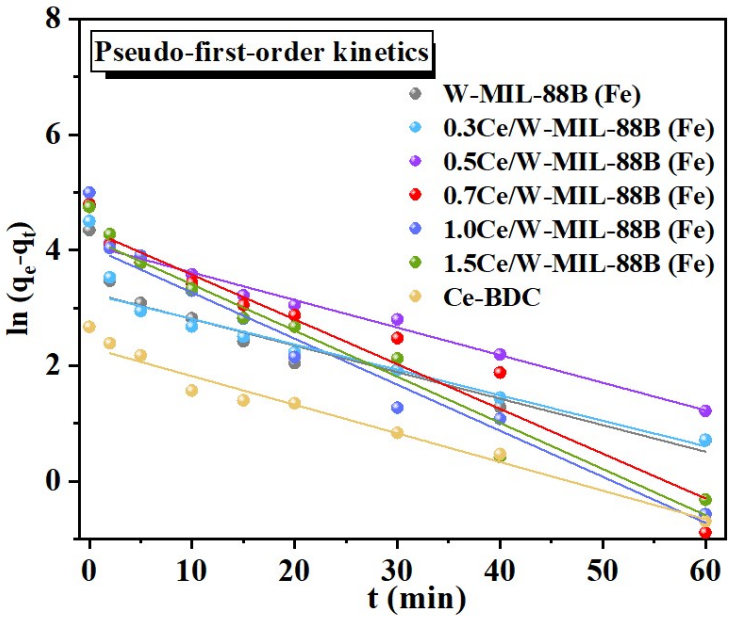

Figure S5. Pseudo-first-order kinetics fitting curve for As(V) adsorption.

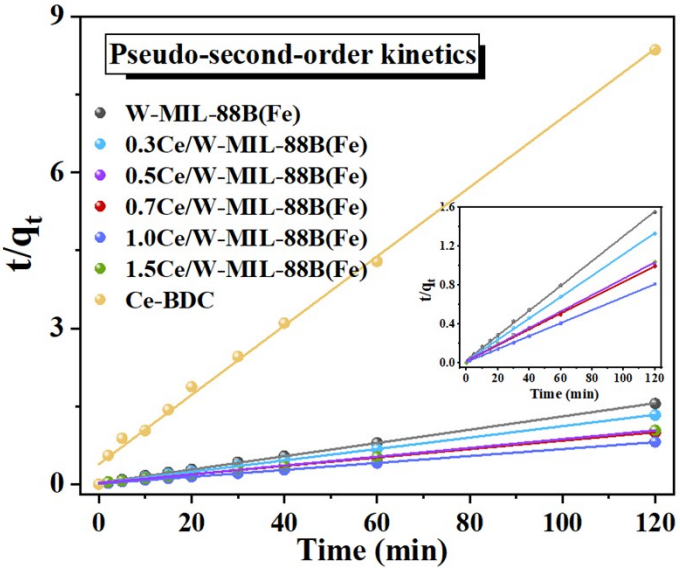

Figure S6. Pseudo-second-order kinetics fitting curve for As(V) adsorption.

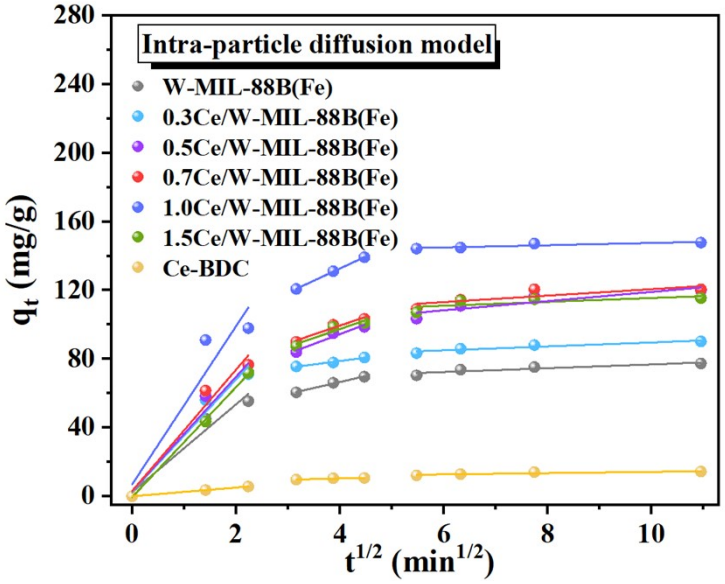

Figure S7. Intra-particle diffusion model fitting curve for As(V) adsorption.

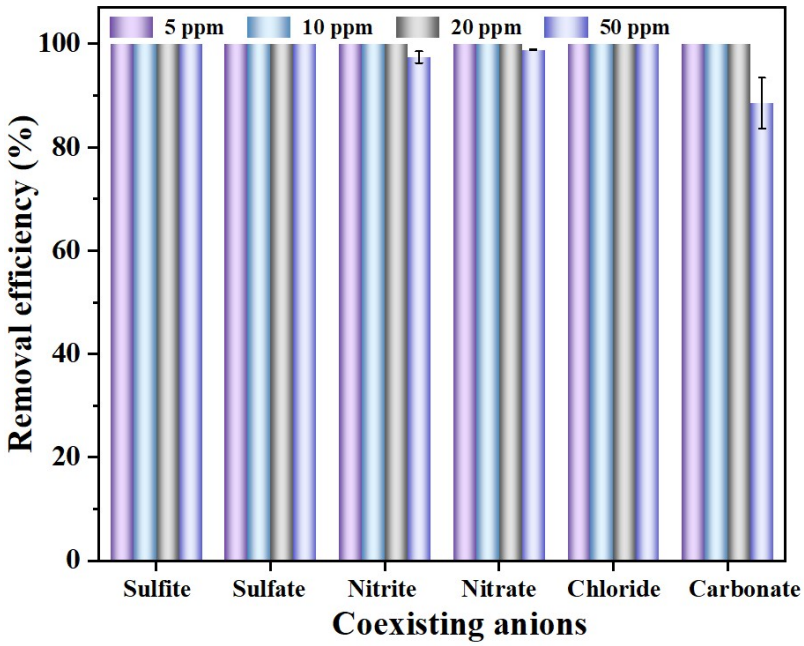

Figure S8. Effects of coexisted ions of different concentrations on As(V) removal efficiency. Experimental conditions: c_{cat} = 0.25 g·L^{-1}, $c_{(As)}$ = 10 mg·L^{-1}, T = 318 K, V = 100 mL, and pH = 7.0.

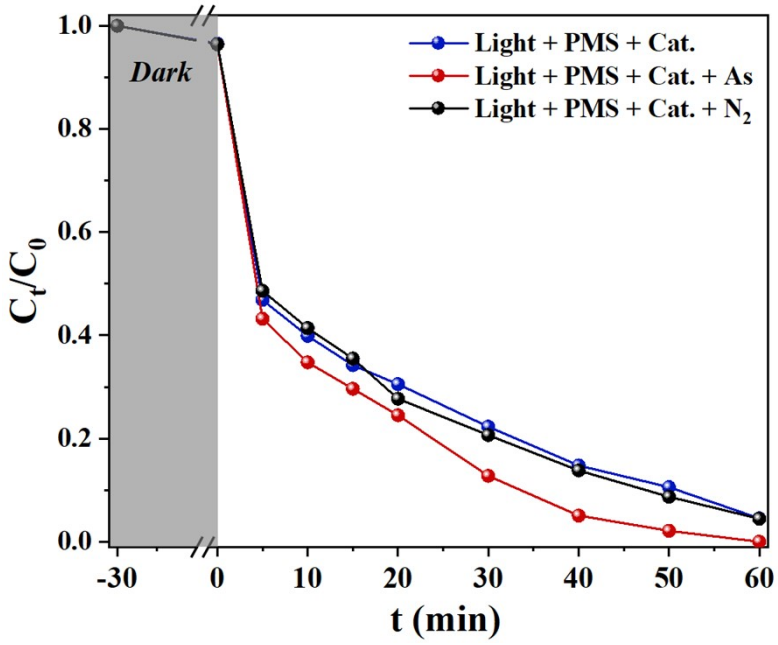

Figure S9. Ce/W-MIL-88B(Fe)-PMS-Light system operates in N_2 atmosphere.

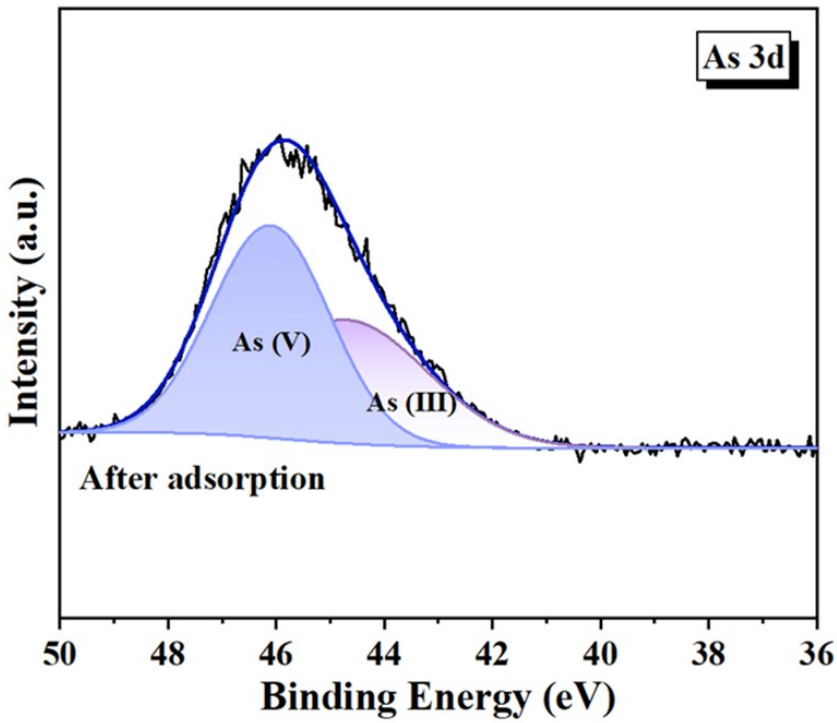

Figure S10. As 3d XPS spectra of Ce/W-MIL-88B(Fe) before and after As(V) adsorption.

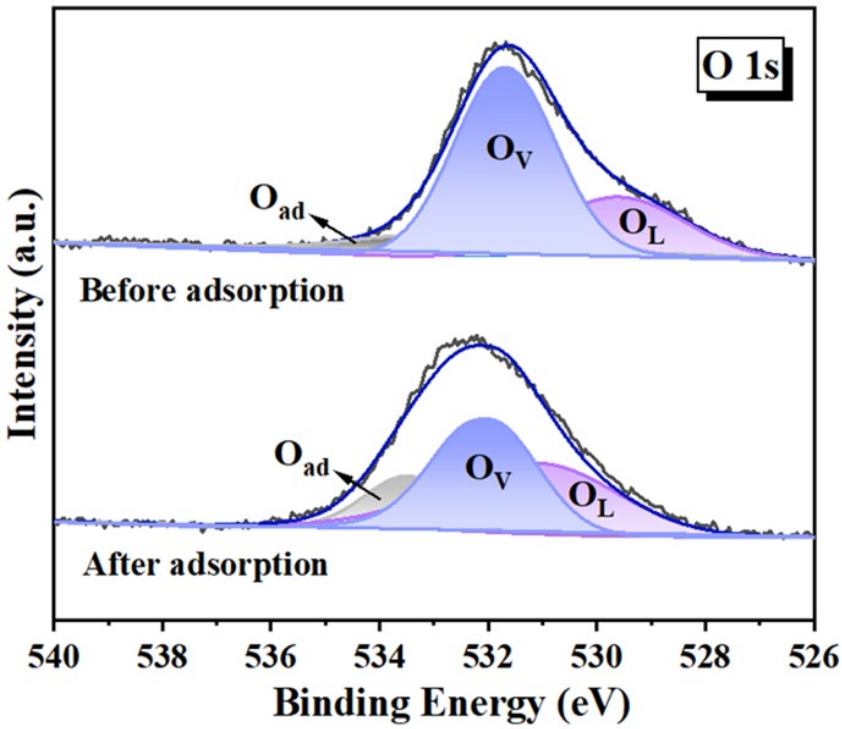

Figure S11. O 1s XPS spectra of Ce/W-MIL-88B(Fe) before and after As(V) adsorption.

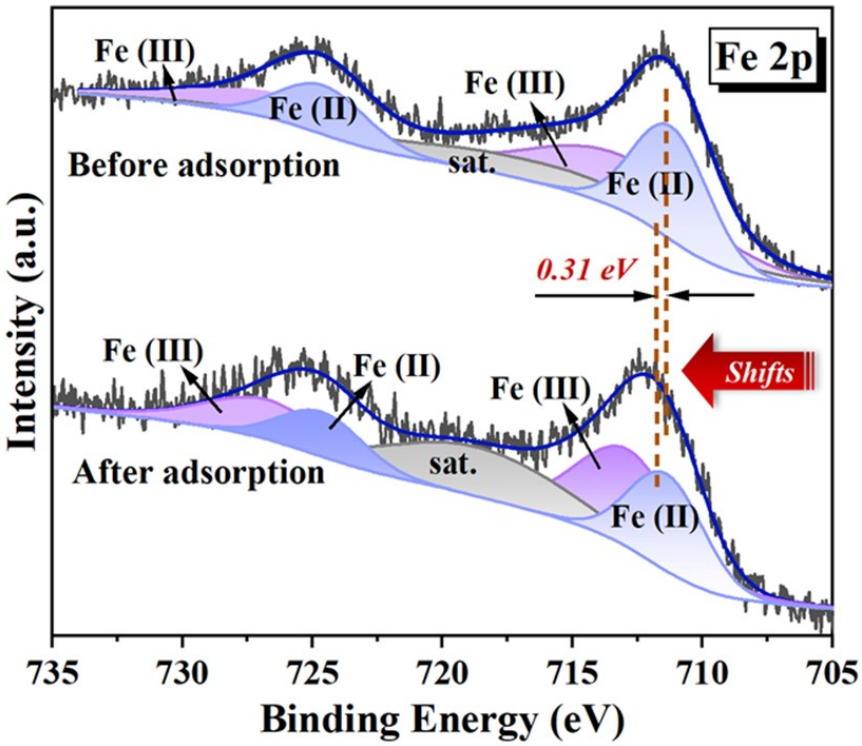

Figure S12. Fe 2p XPS spectra of Ce/W-MIL-88B(Fe) before and after As(V) adsorption.

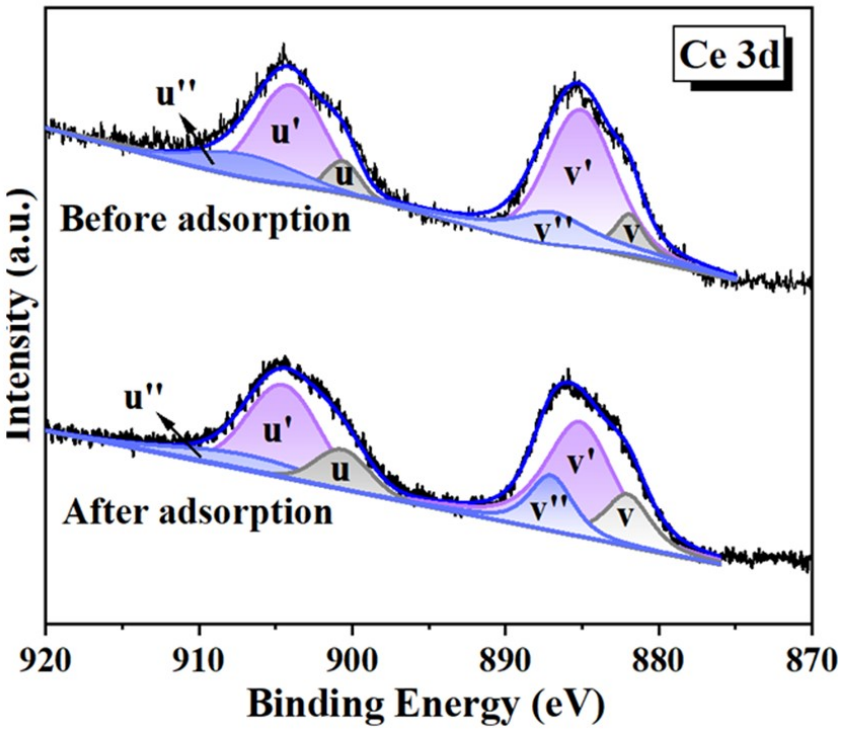

Figure S13. Ce 3d XPS spectra of Ce/W-MIL-88B(Fe) before and after As(V) adsorption.

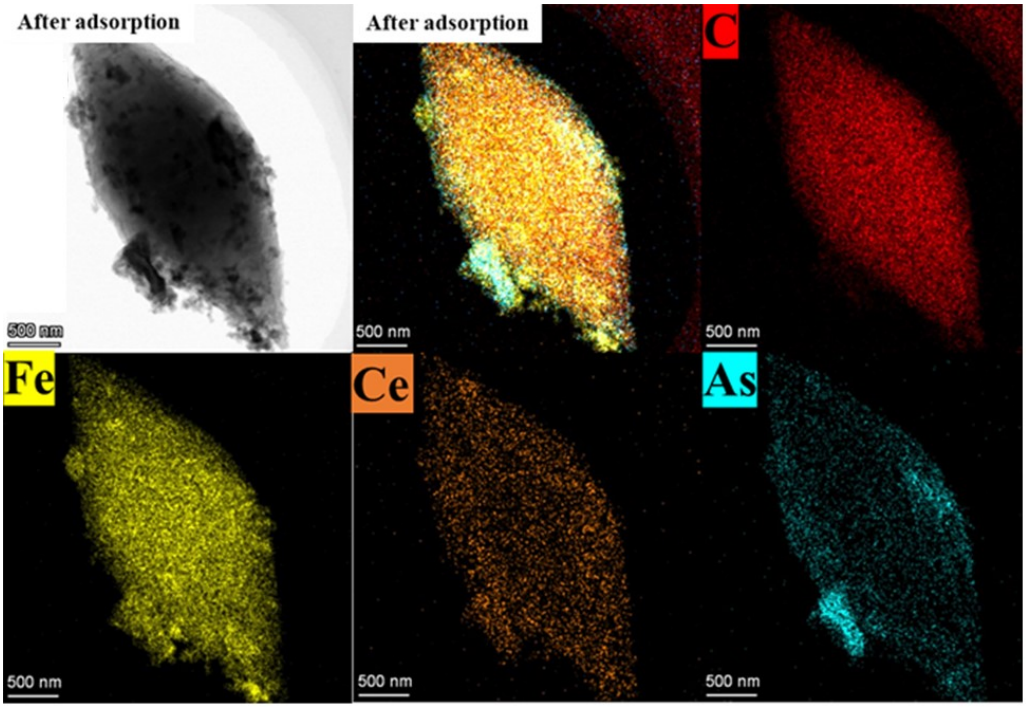

Figure S14. SEM image and EDS images of the used Ce/W-MIL-88B(Fe).

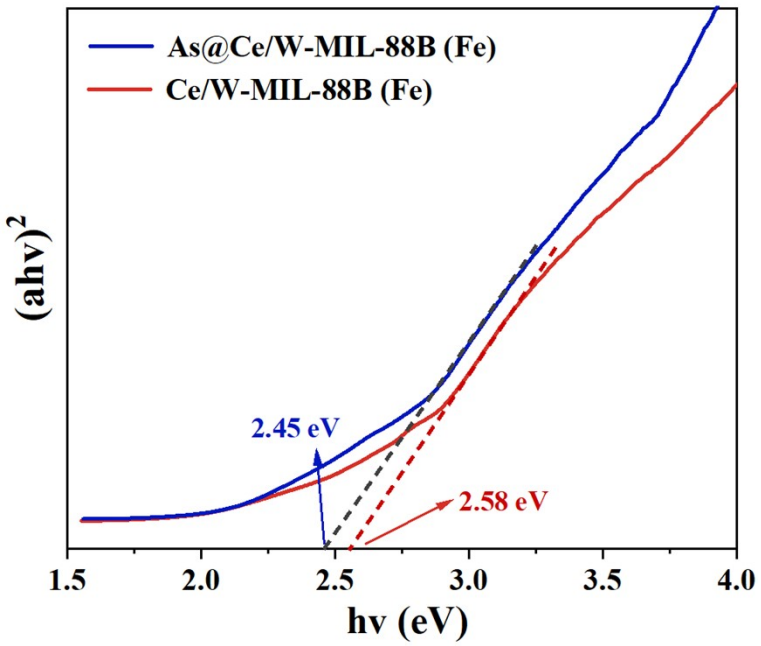

Figure S15. Tauc plots of Ce/W-MIL-88B(Fe) and As@Ce/W-MIL-88B(Fe).

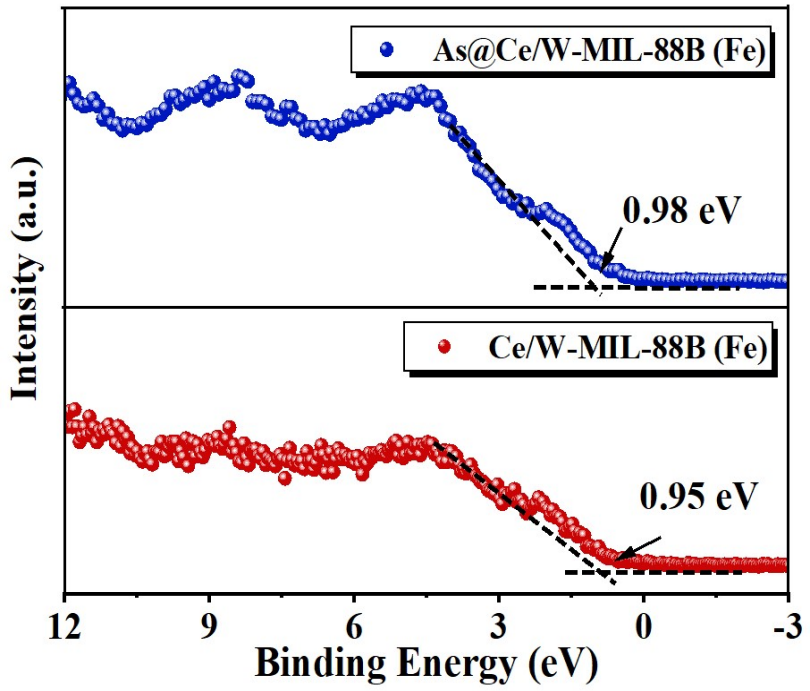

Figure S16. VB-XPS of Ce/W-MIL-88B(Fe) and As@Ce/W-MIL-88B(Fe).

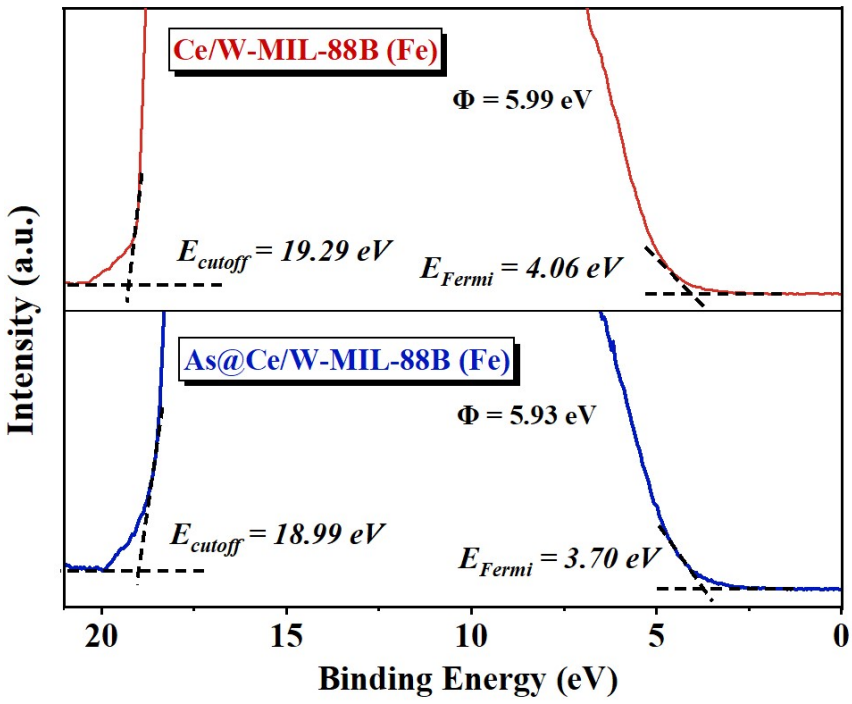

Figure S17. UPS spectra of Ce/W-MIL-88B(Fe) and As@Ce/W-MIL-88B(Fe).

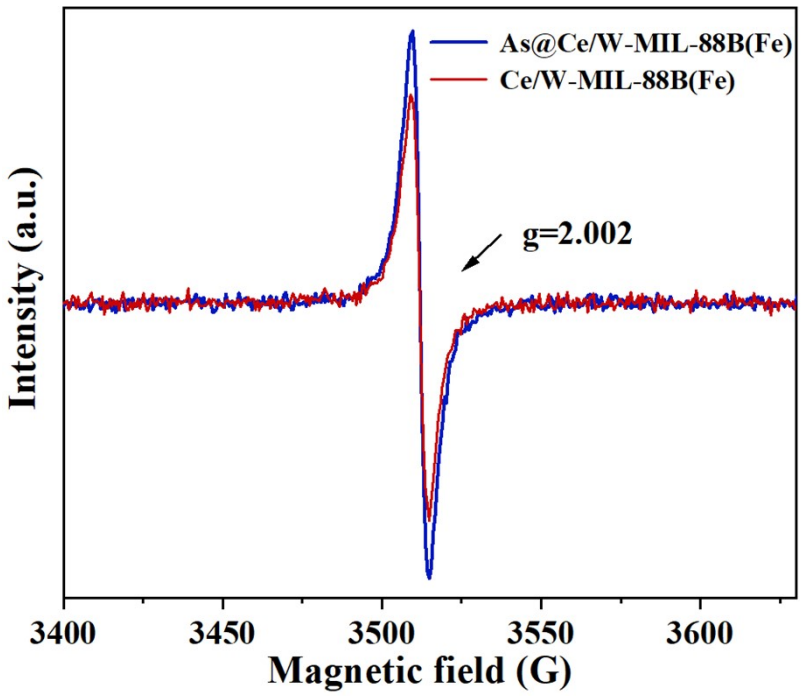

Figure S18. ESR of Ce/W-MIL-88B(Fe) and As@Ce/W-MIL-88B(Fe).

Table S1. Proportions of Fe, Ce, and O species on the surface of five different kinds of catalysts.

Sample	Fe 2p		Ce 3d		O 1s		
	Fe^{2+}/Fe	Fe^{3+}/Fe	Ce^{3+}/Ce	Ce^{4+}/Ce	O_{ad}/O	O_V/O	O_L/O
Ce/W-MIL-88B(Fe)	46.1%	53.9%	65.7%	34.3%	24.4%	61.3%	14.3%
W-MIL-88B(Fe)	37.6%	62.4%	/	/	13.9%	77.5%	8.6%
Ce-BDC	/	/	46.7%	53.3%	/	/	/

Table S2. Parameters of adsorption kinetics for As(V) adsorption.

		Composites						
		W-MIL-88B(Fe)	**0.3**	**0.5**	**0.7**	**1**	**1.5**	**Ce-BDC**
Pseudo-first -order	$q_{e,cal}$(mg·g^{-1})	26.31	25.79	26.31	77.48	57.97	67.36	10.07
	$k_1\times10^{-1}$ (min^{-1})	0.46	0.44	0.48	0.77	0.80	0.80	0.50
	R^2	0.955	0.964	0.989	0.940	0.977	0.966	0.977
Pseudo-second -order	$q_{e,cal}$(mg·g^{-1})	78.25	90.99	118.20	123.15	149.92	117.65	15.02
	$k_2\times10^{-2}$(g·(mg·min)$^{-1}$)	0.60	0.62	0.33	0.30	0.43	0.39	1.15
	R^2	0.999	0.999	0.999	0.999	0.999	0.998	0.996
Intra-Particle diffusion model	k_1(mg·g^{-1}·min$^{-1/2}$)	25.56	32.66	33.31	35.30	46.05	32.03	2.25
	R^2	0.961	0.971	0.965	0.966	0.907	0.999	0.999
	k_2(mg·g^{-1}·min$^{-1/2}$)	6.96	3.97	11.41	10.29	14.12	10.41	0.74
	R^2	0.993	0.987	0.951	0.993	0.999	0.901	0.927
	k_3(mg·g^{-1}·min$^{-1/2}$)	1.11	1.15	2.86	1.88	0.65	1.13	0.37
	R^2	0.838	0.885	0.803	0.667	0.808	0.500	0.814

Table S3. Langmuir and Freundlich isotherm fitting parameters for As(V) adsorption on Ce/W-MIL-88B(Fe).

Composite	Langmuir				Freundlich		
	q_m(mg·g^{-1})	Actual q_m(mg·g^{-1})	K_L(L·mg^{-1})	R^2	K_F (mg$^{1-(1/n)}$L$^{1/n}$ g^{-1})	R^2	n
Ce/W-MIL-88B(Fe).	183.39	181.01	0.87	0.979	120.82	0.817	10.46

Table S4. Proportions of Fe and O species on the surface of Ce/W-MIL-88B(Fe) before and after catalysis.

Sample	Fe 2p		O 1s		
	Fe^{2+}/Fe	Fe^{3+}/Fe	$O_{\alpha d}$/O	O_V/O	O_L/O
Before catalysis	46.0%	54.0%	14.3%	61.3%	24.4%
After catalysis	58.6%	41.4%	23.9%	66.5%	6.6%

Table S5. Proportions of Fe, O, and As species on the surface of Ce/W-MIL-88B(Fe) before and after adsorption.

Sample	Fe 2p		As 3d		O 1s		
	Fe^{2+}/Fe	Fe^{3+}/Fe	As^{3+}/As	As^{5+}/As	$O_{\alpha d}$/O	O_V/O	O_L/O
Before adsorption	46.0%	54.0%	/	/	14.3%	61.3%	24.4%
After adsorption	39.3%	60.7%	44.5%	55.5%	22.1%	47.8%	30.1%

Table S6. Proportions of Fe, O, and As species on the surface of Ce/W-MIL-88B(Fe) before and after simultaneous catalytic NO_2^- oxidation and As(V) adsorption.

Sample	Fe 2p		As 3d		O 1s		
	Fe^{2+}/Fe	Fe^{3+}/Fe	As^{3+}/As	As^{5+}/As	$O_{\alpha d}/O$	O_V/O	O_L/O
Fresh	46.0%	54.0%	/	/	14.3%	61.3%	24.4%
Used	66.7%	33.3%	/	100.0%	18.6%	55.4%	26.0%

References

1. S. Rojas-Buzo, P. Concepcion, J. Luis Olloqui-Sariego, M. Moliner and A. Corma, Metalloenzyme-Inspired Ce-MOF Catalyst for Oxidative Halogenation Reactions, *ACS Appl. Mater. Interfaces*, 2021, **13**, 31021-31030.
2. A. Kuila and P. Saravanan, Intramolecular orbital engineered hetero bimetallic Ce-Fe MOF with reduced transition energy and enhanced visible light property, *Appl Organomet Chem*, 2020, **34**.